Icarus **142**, 342–356 (1999)
Article ID icar.1999.6228, available online at http://www.idealibrary.com on IDEAL®

Ammonia and Eddy Mixing Variations in the Upper Troposphere of Jupiter from HST Faint Object Spectrograph Observations[1]

S. G. Edgington[2] and S. K. Atreya

Department of Atmospheric, Oceanic, and Space Sciences, University of Michigan, Ann Arbor, Michigan 48109–2143
E-mail: sgest@engin.umich.edu

L. M. Trafton

McDonald Observatory, University of Texas, Austin, Texas 78712

J. J. Caldwell

Department of Physics and Astronomy, York University, North York, ON, M35 1P3, United Kingdom

R. F. Beebe and A. A. Simon[3]

Astronomy Department, New Mexico State University, Las Cruces, New Mexico 88033

and

R. A. West

Jet Propulsion Laboratory, California Institute of Technology, 4800 Oak Grove Drive, Pasadena, California 91109

Received January 6, 1999; revised August 30, 1999

Ultraviolet spectra of the northern and southern hemispheres of Jupiter taken with the Hubble Space Telescope Faint Object Spectrograph (FOS) in May 1992 and June 1993 have been used to derive the altitude profiles of NH_3 in the vicinity of the tropopause. For a given pressure level, it is shown that the vertical profile of ammonia varies with latitude and the atmospheric feature being observed. The mixing ratio of ammonia present above the Great Red Spot (GRS) is 8×10^{-8} at 250 mbar, whereas it is four times greater in the nearby South Equatorial Belt at the same pressure level. Our findings agree with those of C. A. Griffith, B. Bézard, T. Owen, and D. Gautier (1992, *Icarus* **98, 82–93), who find NH_3 to be depleted over the GRS with respect to the South Tropical Zone at the time of the Voyager encounters. Variations of the ammonia mixing ratio in the northern and southern hemispheres are found to be nonmonotonic in latitude, indicating local dynamical effects. The observed latitudinal variation of the altitude profile of NH_3 is likely to be caused by variations in the vertical eddy mixing (K), which competes with the photolysis and condensation losses of NH_3. We also find this vertical mixing to be nonmonotonic with latitude. Instead, it shows high variability depending on the region and feature observed, consistent with the values of eddy mixing derived by L.-M. Lara, B. Bézard, C. A. Giffith, J. H. Lacy, and T. Owen (1998,** *Icarus* **131, 317–333). Values at 13°N, 18°N, at the equator, and over the Great Red Spot region range between 3 and 10×10^3 cm^2 s^{-1} at 250 mbar, while weaker mixing occurs at 20°S, 33°S, and 7°N ($<1 \times 10^3$ cm^2 s^{-1} at 250 mbar). Typically, the eddy mixing profiles have a ledge-like vertical structure, where a large mixing coefficient is required below the photolysis region ($p \geq 300$ mbar), followed by a drop to a minimum as we proceed to lower pressures, and finally an increase again with decreasing pressure. In this paper, we also update our previous results on NH_3 and K following the recalibration of the FOS data using the most recent recommendations of the Space Telescope Science Institute.**

Key Words: **Jupiter, atmosphere; photochemistry; radiative transfer; spectroscopy; ultraviolet observations.**

INTRODUCTION

Observation of various constituents in planetary atmospheres can provide valuable information about the chemical and dynamical processes occurring in their atmospheres. These processes can manifest themselves differently in the form of the spatial distribution of constituents depending on the region of the

[1] Based on observations with the NASA/ESA Hubble Space Telescope, obtained at the Space Telescope Science Institute, which is operated by the Association of Universities for Research in Astronomy, Inc., under NASA Contract NAS5-26555.

[2] Present address: Jet Propulsion Laboratory, M/S 169-237, 4800 Oak Grove Drive, Pasadena, CA 91109.

[3] Present address: Cornell University, 326 Space Sciences Building, Ithaca, NY 14853.

0019-1035/99 $30.00

atmosphere being observed and the sources of energy that drive the chemistry and dynamics. To aid in studying these processes, in addition to having a knowledge of the globally averaged vertical distribution of species, it is important to extend this knowledge to their variation in both altitude and latitude.

In Edgington *et al.* (1997), hereafter called Paper I, we presented results derived from ultraviolet (180–230 nm) spectra of Jupiter's northern hemisphere taken in May 1992 by the Faint Object Spectrograph (FOS) onboard the Hubble Space Telescope (HST). These data revealed that the UV albedo (reflectance) varied with latitude, thus indicating local changes in the height distribution of ammonia. The altitude profile of ammonia was derived at each observed latitude using a one-dimensional photochemical model combined with a multiple scattering radiative transfer model to self-consistently generate synthetic fits to the albedos. These profiles were found to vary with latitude, where, of the regions observed, the largest NH_3 mixing ratio was observed at 6°N (2×10^{-9} at 100 mbar) and the smallest at 25°N (3.5×10^{-10} at 100 mbar).[4]

Through the use of the photochemical model (see Paper I), which combines the hydrocarbon, ammonia, and phosphine photochemical families, the vertical eddy mixing coefficients necessary for reproducing the derived ammonia distributions were also inferred. The density distribution of ammonia is highly sensitive to the eddy mixing coefficient which, along with chemical recycling, is necessary to balance the destruction of gas-phase NH_3 due to photolysis and condensation in such a manner as to reproduce the observed albedos. From this analysis, the eddy mixing was also found to vary with latitude, with the region of strongest vertical mixing being located at 6°N (3×10^3 cm^2 s^{-1} at 130 mbar) and decreasing slightly toward midlatitudes (1.4×10^3 cm^2 s^{-1} at 130 mbar). Unfortunately, at high latitudes (i.e., 48°N and 65°N), aerosols to a large extent mask the ammonia absorption, thus preventing reliable ammonia and eddy mixing profiles from being derived.

Also presented in Paper I were upper limits on the mixing ratio of phosphine. The phosphine absorption cross section has a broad continuum at wavelengths >160 nm (Chen *et al.*, 1991), making it difficult to distinguish phosphine from the effects of aerosols and other continuum absorbers. Hence, PH_3 cannot be uniquely identified in the FOS reflectance unless it is present in large abundances and prevents accurate abundances from being obtained. Phosphine profiles obtained from photochemical modeling were found to be confined to altitudes below the region of ammonia photolysis. While the photolysis of phosphine takes place throughout the stratosphere and upper troposphere, due to the smaller abundance of phosphine in the troposphere compared with that of ammonia (solar $P/N = 3.33 \times 10^{-3}$), the absorption optical depth of phosphine at all relevant wavelengths is unity at a deeper level of the atmosphere compared with the level at which the ammonia optical depth reaches unity. Thus, maximum photolysis of phosphine takes place deeper in the atmosphere and does not contribute greatly to the opacity between 180 and 230 nm when compared with the opacities of ammonia and acetylene. A distribution of phosphine was derived by assuming that PH_3 can provide the opacity longward of 220 nm, where ammonia has weaker absorption and acetylene absorption is greatly diminished. This profile has a substantial PH_3 abundance extending to higher altitudes (see Fig. 6 of Paper I) and essentially gives an upper limit to the amount of phosphine present in the troposphere. However, it was noted that aerosols may provide a strong source of opacity in this region.

Finally, only estimates of the acetylene mixing ratio were obtained due to large uncertainties in the FOS continuum below 180 nm caused by stray photons scattered from longer wavelengths within the instrument, which are typically referred to as grating scattered light (Cunningham and Caldwell, 1993). This large uncertainty made it impossible to obtain an altitude distribution of acetylene, since inadequate subtraction of the excess photons from the FOS data can lead to large errors in the determination of the C_2H_2 mixing ratio.

In this paper, we present the variation of the ammonia mixing ratio and the eddy mixing coefficient (K) with altitude and latitude as derived from the FOS spectra taken the following year of the northern and southern hemispheres of Jupiter along the central meridian longitude (CML). Included in this analysis are spectra of the Great Red Spot (GRS) and the nearby South Equatorial Belt (SEB). Results from these data sets are then compared with those based on data presented in Paper I, which have been reanalyzed based on improved pointing estimates and the latest calibrations, to gain an understanding of the variation of NH_3 and K over much of the planet. To this extent, the values presented in this paper update those presented in Paper I. Given the uncertainties in determining C_2H_2 and PH_3 mixing ratios, we focus only on ammonia which provides the dominant source of opacity between 200 and 220 nm and whose spectral signature in the FOS data is quite unambiguous.

DATA REDUCTION AND METHOD OF ANALYSIS

The spectral data presented here were taken of the northern and southern hemispheres (72°N, 43°N, 7°N, Equator, 6°S, 10°S, 20°S, 33°S, 43°S, 67°S) of Jupiter with the FOS during Cycle 2 of the HST (July 5 and 6, 1993). Exceptions to these are the spectra of the GRS and the nearby SEB ($\Delta\lambda \approx 23$), which were taken during Cycle 1 (May 19 and 20, 1992, respectively). The rest of the Cycle 1 data covering 13°N–43°N have been presented in Paper I and are reanalyzed here. The Cycle 2 data were taken using the G190H grating, which covers the wavelength range of 160–230 nm, and the Amber detector, which has relatively high sensitivity. The integration time for data

[4] As a result of improving our pointing estimates for the observations, several latitudes were found to be different from the nominal positions specified for the observation. The largest discrepancy occurs for the two spectra referred to as 6°N in Edgington *et al.* (1997) as these actually were actually found to correspond to 13°N and 15°N. Following the Introduction, we refer to the corrected values for the observations. (See Table I for the exact latitudes and longitudes of the observations.)

TABLE I
Observation Details

Region of Observation	Original Designation	Date (MM/DD/YY)	Time (UT)	Exposure Time (min)/ Aperture Size (arc sec)	Latitude/ Δ Longitude from CML (Sys III)	Sub-Earth Pt. (Sys III)	Sub-Solar Pt. (Sys III)
			Cycle 1				
GRS	GRS	05/19/92	07:27:29	24,0.5	18.91S,36.9	-1.30,215.94	-1.72,205.26
SEB	SEB	05/20/92	14:00:36	24,0.5	17.03S,-14.4	-1.30,243.96	-1.72,233.25
15 N	6 N	05/21/92	22:38:39	15,1.0	15.27N,0.26	-1.30,347.49	-1.73,336.75
13 N	6 N	05/21/92	23:49:09	15,1.0	13.66N,-0.69	-1.30,30.10	-1.73,19.37
18 N	15 N	05/25/92	04:59:57	24,1.0	17.98N,-1.79	-1.30,309.13	-1.74,298.36
15 N	20 N	05/26/92	06:43:31	24,1.0	15.60N,1.35	-1.29,162.11	-1.74,151.34
22 N	25 N	05/20/92	04:37:54	24,1.0	22.08N,-1.21	-1.30,263.84	-1.72,253.13
43 N	48 N	05/22/92	04:58:50	15,1.0	42.59N,-0.67	-1.30,217.28	-1.73,206.55
45 N	48 N	05/22/92	06:15:03	15,1.0	45.40N,-3.71	-1.30,263.35	1.73,252.62
61 N	65 N	05/22/92	12:44:35	15,1.0	61.22N,-31.9	-1.30,138.80	-1.73,128.06
66 N	65 N	05/22/92	13:05:32	15,1.0	65.94N,28.0	-1.30,151.47	-1.73,140.72
			Cycle 2				
72 N	65 N	06/06/93	06:15:40	15,1.0	72.24 N	-2.77,199.08	-3.02,188.96
43 N	48 N	06/06/93	07:50:15	15,1.0	43.53 N	-2.77,256.25	-3.02,246.13
7 N	6 N	06/05/93	23:48:17	15,1.0	7.59 N, 30	-2.77,324.91	-3.02,314.81
EQ	Equator	06/05/93	22:11:52	15,1.0	2.66 S	-2.77,266.63	-3.02,256.53
6 S	6 S	06/05/93	20:37:43	15,1.0	5.82 S	-2.77,209.72	-3.02,199.62
10 S	12 S	06/06/93	01:24:41	15,1.0	10.53 S	-2.77,23.19	-3.02,13.08
20 S	25 S	06/06/93	09:29:34	15,1.0	20.43 S, 30	-2.77,316.29	-3.02,306.16
33 S	33 S	06/06/93	11:03:02	15,1.0	33.48 S	-2.77,12.78	-3.02,2.65
43 S	48 S	06/06/93	03:01:03	15,1.0	43.31 S	-2.77,81.44	-3.02,71.32
67 S	65 S	06/06/93	04:37:27	15,1.0	66.78 S	-2.77,139.71	-3.02,129.59

accumulation was 15 min for all spectra except those of the GRS and SEB, for which it was 24 min due to the use of a smaller aperture. Detailed information about the ephemeris and instrument settings for these observations are given in Table I. Refined pointing information was obtained by mapping the right ascension/declination of the observations onto an oblate spheroid representing Jupiter as seen in images taken with the Wide Field Planetary Camera during the same observing program. In this paper, we use the nomenclature listed in the first column of Table I to refer to the observations of specific regions.

The physical quantity measured by the FOS is the flux of light coming from Jupiter within a particular solid angle as determined by the aperture size chosen for making the observations (see Table I). This flux is then corrected for instrumental effects including grating scattered light and flat fielding (Ford 1985). We have used the latest calibration files recommended by the Space Telescope Science Institute for each of the Cycle 1 and 2 datasets. This leads to a ∼10% increase in the albedo relative to those presented in Paper I. Dividing the measured flux by the solid angle gives an intensity, which is then divided by F to obtain the albedo (reflectance), where πF is the solar flux at the time of the observations scaled to the distance of Jupiter. This removes trends due to solar features (with the exception of ghost features arising from Raman scattering), thus leaving information only about the absorption and scattering properties of the planet itself.

The solar spectrum used here is the SUSIM solar spectrum measured onboard the Space Shuttle with a resolution of 0.05 nm (van Hoosier *et al.* 1988). This was then normalized to a 1-nm-resolution UARS/SOLSTICE spectrum (obtained from the Distributed Active Archive Center at Goddard Space Flight Center) measured on each day corresponding to the observations. This allowed for correction of the continuum of the SUSIM spectrum to that at the time of the observations. Since the absorbers considered here have broad absorption features at these wavelengths, this is considered adequate for this analysis. For further details about the reduction of these data, the reader is referred to Paper I.

The procedure for determining the altitude variation of the molecular absorbers that give a good fit of the synthetic spectra to each of the FOS spectra has also been given in detail in Paper I. Briefly, given the geometrical parameters of the observations (Table I), a photochemical model, which includes condensation loss, is used to constrain the chemical and radiative properties of the jovian atmosphere, which is assumed to correspond to that determined by the Galileo Probe (Seiff *et al.*, 1997) at all latitudes. Through the specification of the vertical eddy mixing coefficient, an altitude distribution of the mixing ratios of UV-absorbing species is generated by the photochemical model. From this profile, a synthetic albedo is generated by solving the radiative transfer equation for the intensity leaving the jovian atmosphere in the direction of the Earth. In contrast to Paper I, Raman scattering, which acts as an additional source of both opacity and emission, has been rigorously included in our radiative transfer model to account for the redistribution of photons to different wavelengths (see Appendix for further details). This

can act to reduce or increase the number of photons available for scattering out of the atmosphere depending on the wavelength. The vertical mixing coefficient is determined by adjusting K until the synthetic albedo matches the observations, giving valuable first-order information about the dynamics of the atmosphere in the vicinity of the tropopause. Further information on the choice of K is given in the next section.

OBSERVATIONS AND RESULTS

Several of the Cycle 1 and Cycle 2 albedos are shown in Fig. 1. Note that the Cycle 1 albedos are larger by roughly 10% compared with those in Paper I due to the newer calibrations. Since the scattering properties of the atmosphere have not changed, this increased albedo has the effect of shifting the ammonia distribution downward in the atmosphere compared with those presented in Paper I. At 210 nm and for an overhead Sun, the Rayleigh–Raman scattering optical depths of 1, 2, and 3 occur at 142, 278, and 419 mbar, respectively, with the addition of NH_3 increasing the total optical depth at all levels. Thus we consider our results to be most valid from 100 to 275 mbar. Variations of the albedo with latitude and over the GRS region can be noted and most likely result from a combination of latitude variations of the altitude profiles of the absorbing molecules and geometrical viewing effects. Paper I gave a detailed description of the various spectral features in the FOS albedos, so we summarize only the important points here. From these spectra, the absorption features of acetylene and ammonia can be clearly discerned from their unique spectral signatures in the UV, at wavelengths $\leq$210 and $\geq$200 nm, respectively. However, due to grating scattered light, the continuum on which the acetylene spectral signatures rest ($<$190 nm) is uncertain and somewhat subjective, making this region unreliable for determining species mixing ratios. At wavelengths greater than 200 nm, the uncertainty in the continuum is much smaller, making this region highly valuable for determining the altitude profile of ammonia. Beyond 220 nm, the exact source of the continuum level is unknown, with the strongest candidate being aerosols, although other absorbers such as PH_3 may exist (e.g., Dashevsky and Caldwell 1998 and Paper I). Features superimposed on this continuum are due to Raman scattering. [Note that the apparent feature located near 193.5 nm in the Cycle 2 spectra is thought to be an artifact of the FOS instrument.]

The UV albedo variation with latitude seen in the atmosphere of Jupiter is caused by two effects: differences in viewing geometry (e.g., solar zenith and Earth zenith angles) and the vertical distribution of the spectrally absorbing species and aerosols. As shown later, after taking into account the correct geometrical parameters, fitting of the FOS data reveals that a variation of the vertical distribution of the absorbing chemical species, primarily NH_3, with latitude is indeed required to account for the observed albedo latitude variation. In other words, use of the same vertical profile of NH_3 at all latitudes fails to reproduce all of the observed spectra. Thus, it is necessary to generate several ammonia distributions in a systematic fashion and rule out unwanted cases.

The ammonia profiles are sensitive to two free parameters, the first of which is the vertical eddy mixing in the atmosphere. Several families of eddy profiles were used in this analysis. These consisted of profiles in which the mixing coefficients either were altitude independent, followed power laws, or contained a ledge-like transition from low mixing to high mixing within a relatively small altitude region ($<$1 scale height). Using the photochemical transport model, families of ammonia distributions were generated resulting from these eddy profiles. These ammonia profiles were then used to generate a set of synthetic albedos for comparison to the FOS data.

A second important parameter in determining the ammonia distribution is the temperature. This limits the maximum ammonia abundance to the saturation vapor pressure of ammonia and provides an additional loss mechanism against which dynamical mixing must compete. As will be discussed later, adjusting the temperature relative to the nominal temperature profile (an altitude-independent temperature perturbation is assumed), along with the eddy mixing, is actually needed to obtain fits to several of the FOS spectra.

After using the entire set of eddy mixing profiles and temperature perturbations to produce a family of synthetic spectra, visual inspection of these spectra allowed us to choose the cases that best matched the appropriate FOS albedo. Several of these fits are shown in Figs. 2 and 3. The corresponding vertical distributions of NH_3 (hereafter also referred to as the nominal profiles) as a function of latitude are presented in Figs. 4 and 5 (see also Table II). Other distributions of ammonia produce poorer fits to their respective albedos. At pressures greater than 300 mbar, the ammonia profiles follow the saturated vapor pressure curve for a given temperature profile. In all cases, the NH_3 mixing ratio departs from the saturated NH_3 profile in the upper troposphere, since it is being depleted by photolysis. Note that this decrease of the ammonia mixing ratio with increasing altitude combined with the Rayleigh scattering wavelength dependence is the main reason for the lack of an NH_3 signature at wavelengths less than 200 nm even though the NH_3 absorption cross section happens to be strongest (see Paper I). One can also see large latitudinal variations in the ammonia profile amounting to over an order of magnitude in cases.

To determine the sensitivity of the fits to the ammonia mixing ratio, the nominal NH_3 profiles obtained in the above inspection were scaled by a constant factor and the synthetic reflectance spectrum corresponding to the scaled profile was generated. From this exercise, we find that changes larger than $\pm$25–50% in the NH_3 profile produce changes of $\Delta I/F > 0.005$–0.01 in the synthetic albedos and hence depart from the FOS spectra (compare this to the propagated statistical error shown in Fig. 2). Other uncertainties in the NH_3 mixing ratio may also arise due to errors in the measured cross section of NH_3 [$\pm$10% (Chen *et al.* 1999)]. However, since the relative uncertainty of the albedo from latitude to latitude is determined by the propagated

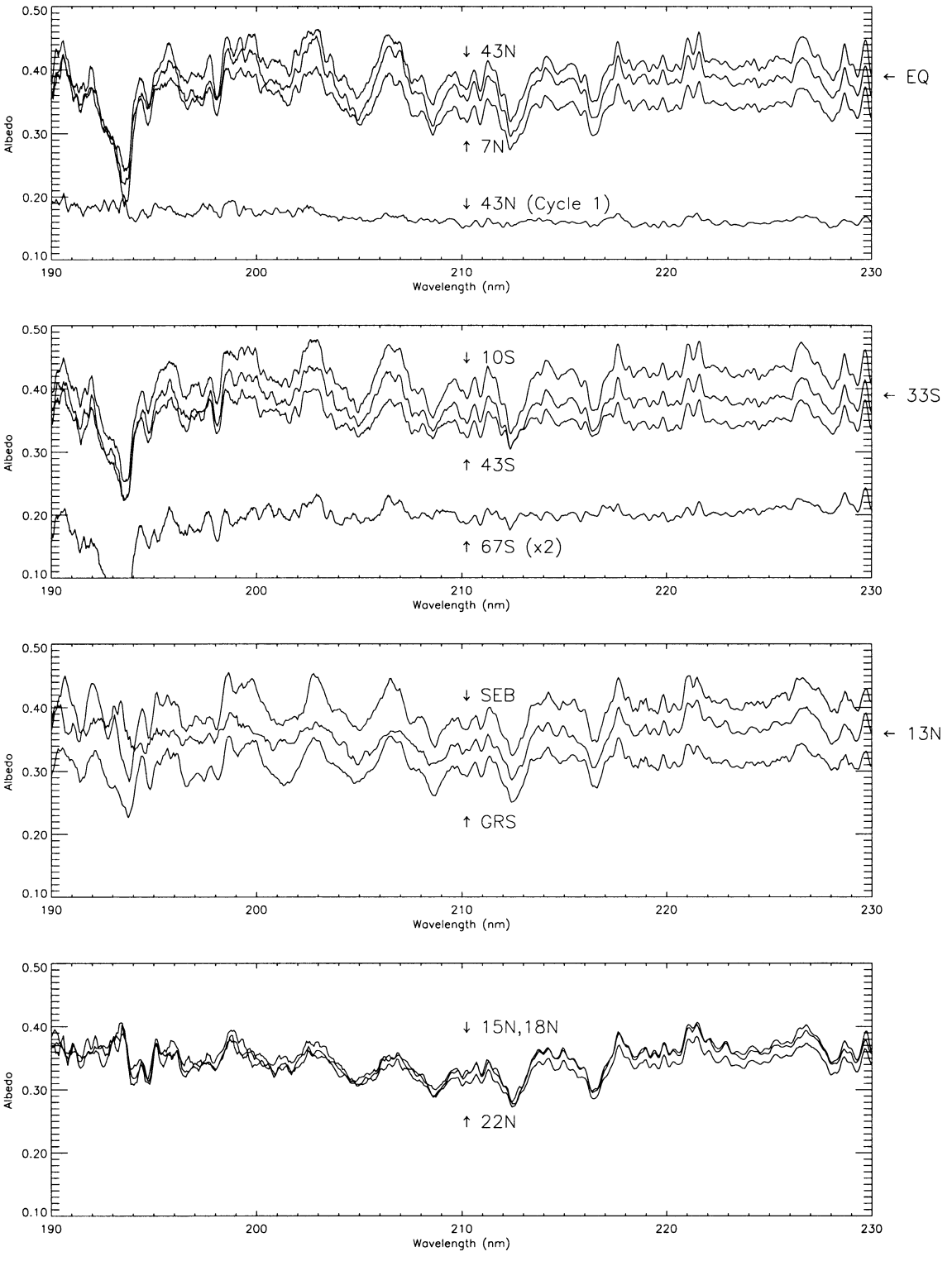

FIG. 1. FOS reflectance spectra taken of several latitudes in the northern and southern hemispheres of Jupiter. The top two panels refer to data taken during Cycle 2 (June 5–6, 1993); the bottom two panels refer to data taken during Cycle 1 (May 19–26, 1992). See Table I for observation information.

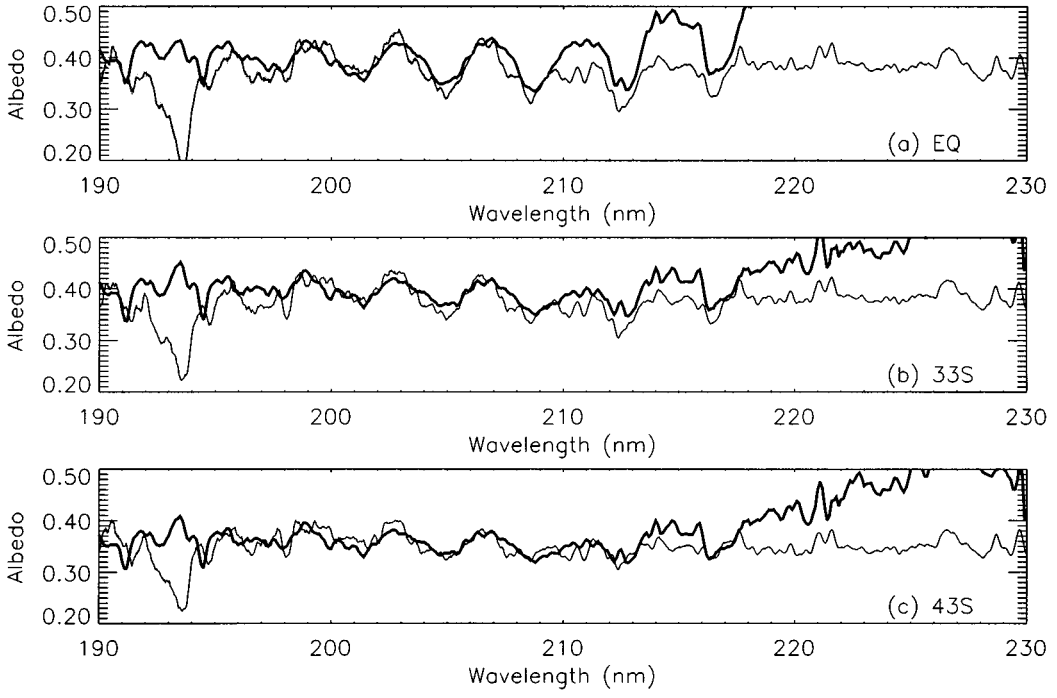

FIG. 2. Synthetic fits (bold lines) of the Cycle 2 FOS reflectances (solid lines) for (a) the Equator, (b) 33°S, and (c) 43°S. (a) also shows the propagated statistical error (gray lines) which is negligible for these observations. Larger errors (∼5–10%) exist in the absolute calibration of the data (see text).

statistical error, which is expected to be small for wavelengths >190 nm, the relative latitudinal changes in the NH_3 mixing ratio (e.g., at corresponding northern and southern latitudes) are expected to have an uncertainty of ±35%. The uncertainty in the absolute calibration of the FOS spectra (∼5–10%) produces a larger uncertainty of a factor of 2–3 for the NH_3 abundance, but will not affect the observed trends.

In the calculation of the synthetic albedos and photolysis rates, the effects of aerosols have been neglected. As illustrated in Paper I (see Figs. 4 and 5 of Paper I), a minimum amount of

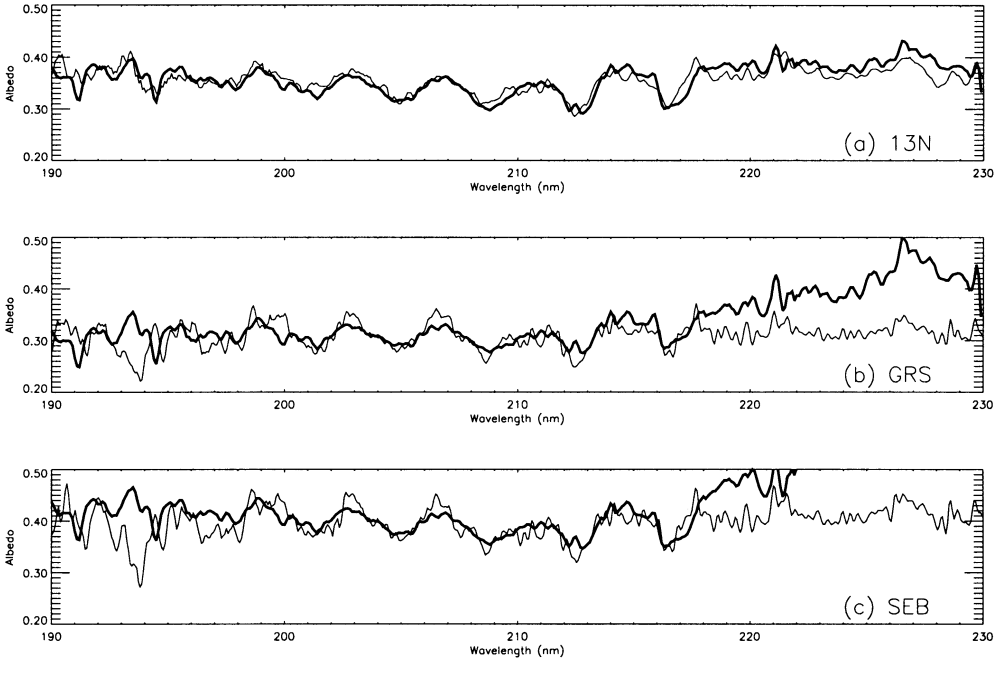

FIG. 3. Synthetic fits (bold lines) of the Cycle 1 FOS reflectances (solid lines) for (a) 13°N, (b) Great Red Spot, and (c) South Equatorial Belt.

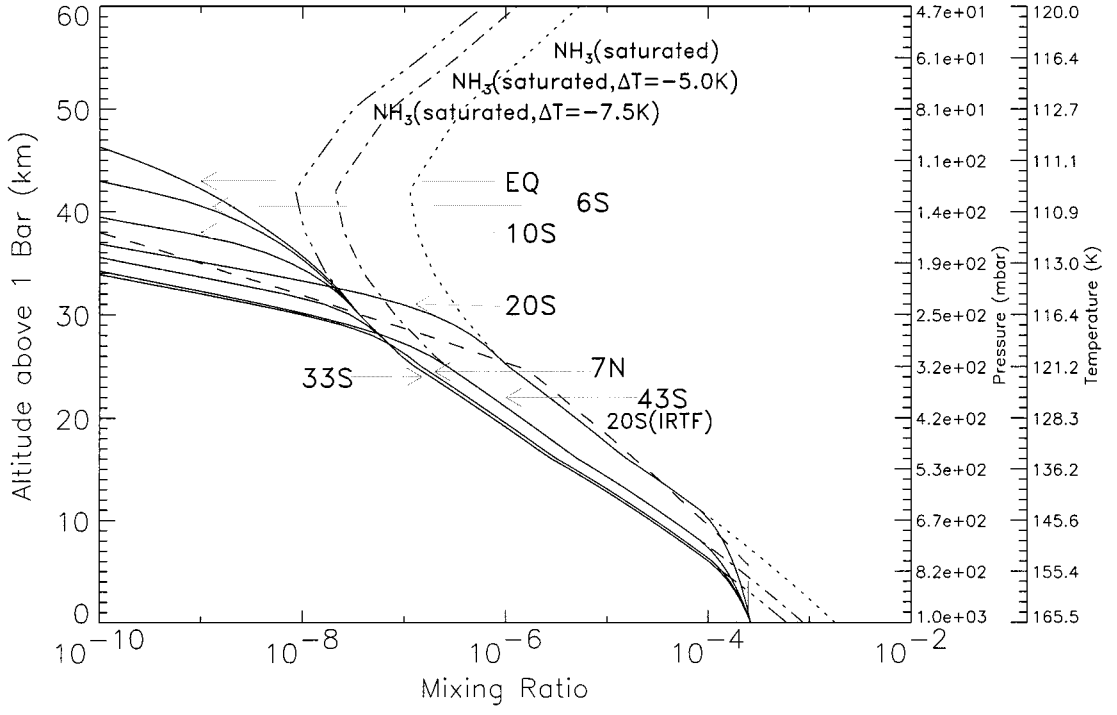

FIG. 4. Variation of the ammonia mixing ratio with altitude for various latitudes on Jupiter as derived from fits of the Cycle 2 FOS spectra. The dotted, dot–dash, and dot–dot–dash curves denote the saturated ammonia mixing ratios corresponding to temperature perturbations of 0, 5, and −7.5 K, respectively, relative to the nominal temperature profile.

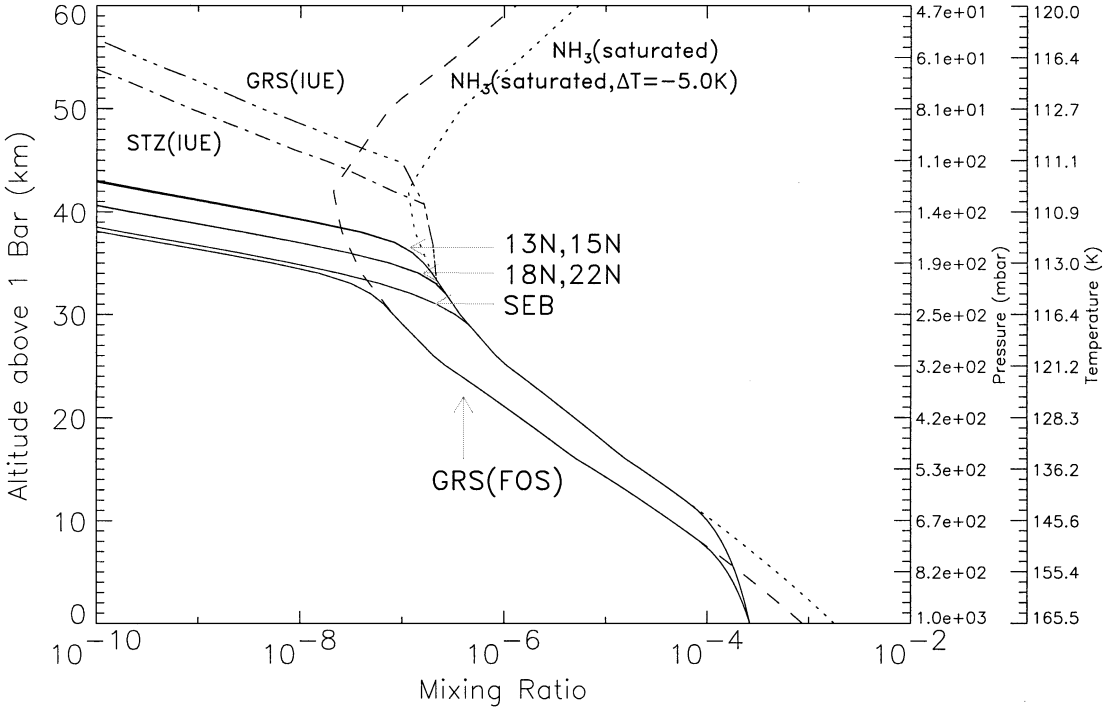

FIG. 5. Variation of ammonia over the Great Red Spot and the South Equatorial Belt. Updated results derived from the Cycle 1 northern hemisphere data are also presented for comparison. Also shown are results derived from IUE observations of the GRS (dash–dot–dot–dot curve) and STZ (dash–dot curve) conducted by Wagener *et al.* (1986) and from IRTF observations of 20°S (dashed curve) conducted by Lara *et al.* (1998). The dotted and dot–dash curves denote the saturated ammonia mixing ratios for temperature perturbations of 0 and −5 K, respectively.

TABLE II

Ammonia Mixing Ratio and Eddy Diffusion Coefficient versus Latitude and Altitude

Latitude (°)	Altitude (km)	Pressure (mbar)	Density (cm^{-3})	NH_3 mixing ratio	Eddy mixing (cm^2s^{-1})
13.0	20.0	4.19e+02	2.37e+19	4.89e-06	1.45e+04
13.0	25.0	3.25e+02	1.94e+19	1.07e-06	1.25e+04
13.0	30.0	2.49e+02	1.55e+19	3.68e-07	8.32e+03
13.0	35.0	1.89e+02	1.21e+19	1.62e-07	2.53e+03
13.0	40.0	1.43e+02	9.33e+18	3.93e-09	5.30e+02
13.0	45.0	1.07e+02	7.00e+18	1.53e-11	5.61e+02
18.0	20.0	4.19e+02	2.37e+19	4.89e-06	1.29e+04
18.0	25.0	3.25e+02	1.94e+19	1.07e-06	9.22e+03
18.0	30.0	2.49e+02	1.55e+19	3.68e-07	3.87e+03
18.0	35.0	1.89e+02	1.21e+19	7.50e-08	4.67e+02
18.0	40.0	1.43e+02	9.33e+18	2.11e-10	4.59e+02
18.0	45.0	1.07e+02	7.00e+18	3.93e-12	5.35e+02
15.0	20.0	4.19e+02	2.37e+19	4.89e-06	1.45e+04
15.0	25.0	3.25e+02	1.94e+19	1.07e-06	1.25e+04
15.0	30.0	2.49e+02	1.55e+19	3.68e-07	8.32e+03
15.0	35.0	1.89e+02	1.21e+19	1.62e-07	2.53e+03
15.0	40.0	1.43e+02	9.33e+18	4.38e-09	5.30e+02
15.0	45.0	1.07e+02	7.00e+18	1.70e-11	5.61e+02
22.0	20.0	4.19e+02	2.37e+19	4.89e-06	1.29e+04
22.0	25.0	3.25e+02	1.94e+19	1.07e-06	9.22e+03
22.0	30.0	2.49e+02	1.55e+19	3.68e-07	3.87e+03
22.0	35.0	1.89e+02	1.21e+19	7.41e-08	4.67e+02
22.0	40.0	1.43e+02	9.33e+18	2.22e-10	4.59e+02
22.0	45.0	1.07e+02	7.00e+18	4.02e-12	5.35e+02
SEB	20.0	4.19e+02	2.37e+19	4.89e-06	9.08e+03
SEB	25.0	3.25e+02	1.94e+19	1.07e-06	2.51e+03
SEB	30.0	2.49e+02	1.55e+19	3.28e-07	4.78e+02
SEB	35.0	1.89e+02	1.21e+19	8.18e-09	4.52e+02
SEB	40.0	1.43e+02	9.33e+18	2.13e-11	4.58e+02
SEB	45.0	1.07e+02	7.00e+18	1.42e-12	5.35e+02
GRS	20.0	4.19e+02	2.37e+19	1.43e-06	1.29e+04
GRS	25.0	3.25e+02	1.94e+19	2.68e-07	9.22e+03
GRS	30.0	2.49e+02	1.55e+19	8.12e-08	3.87e+03
GRS	35.0	1.89e+02	1.21e+19	5.31e-09	4.67e+02
GRS	40.0	1.43e+02	9.33e+18	1.67e-11	4.59e+02
GRS	45.0	1.07e+02	7.00e+18	1.44e-12	5.35e+02
7.0	20.0	4.19e+02	2.37e+19	8.47e-07	9.08e+03
7.0	25.0	3.25e+02	1.94e+19	1.49e-07	2.51e+03
7.0	30.0	2.49e+02	1.55e+19	9.67e-09	4.78e+02
7.0	35.0	1.89e+02	1.21e+19	3.09e-11	4.52e+02
7.0	40.0	1.43e+02	9.33e+18	1.95e-12	4.58e+02
7.0	45.0	1.07e+02	7.00e+18	2.73e-13	5.35e+02
EQ	20.0	4.19e+02	2.37e+19	7.42e-07	1.41e+04
EQ	25.0	3.25e+02	1.94e+19	1.28e-07	1.19e+04
EQ	30.0	2.49e+02	1.55e+19	3.62e-08	1.01e+04
EQ	35.0	1.89e+02	1.21e+19	1.20e-08	8.68e+03
EQ	40.0	1.43e+02	9.33e+18	2.45e-09	7.14e+03
EQ	45.0	1.07e+02	7.00e+18	2.34e-10	3.04e+03
-6.0	20.0	4.19e+02	2.37e+19	7.42e-07	1.38e+04
-6.0	25.0	3.25e+02	1.94e+19	1.28e-07	1.13e+04
-6.0	30.0	2.49e+02	1.55e+19	3.62e-08	9.20e+03
-6.0	35.0	1.89e+02	1.21e+19	1.10e-08	7.24e+03
-6.0	40.0	1.43e+02	9.33e+18	1.44e-09	2.50e+03
-6.0	45.0	1.07e+02	7.00e+18	1.53e-11	5.20e+02
-10.0	20.0	4.19e+02	2.37e+19	7.42e-07	1.45e+04
-10.0	25.0	3.25e+02	1.94e+19	1.28e-07	1.25e+04
-10.0	30.0	2.49e+02	1.55e+19	3.62e-08	8.32e+03
-10.0	35.0	1.89e+02	1.21e+19	7.56e-09	2.53e+03
-10.0	40.0	1.43e+02	9.33e+18	5.46e-11	5.30e+02
-10.0	45.0	1.07e+02	7.00e+18	2.72e-12	5.61e+02
-20.0	20.0	4.19e+02	2.37e+19	4.89e-06	7.00e+02
-20.0	25.0	3.25e+02	1.94e+19	1.07e-06	2.97e+02
-20.0	30.0	2.49e+02	1.55e+19	1.87e-07	3.40e+02
-20.0	35.0	1.89e+02	1.21e+19	1.12e-09	3.95e+02
-20.0	40.0	1.43e+02	9.33e+18	6.73e-12	4.64e+02
-20.0	45.0	1.07e+02	7.00e+18	6.92e-13	5.54e+02
-33.0	20.0	4.19e+02	2.37e+19	7.42e-07	1.24e+04
-33.0	25.0	3.25e+02	1.94e+19	1.28e-07	7.50e+03
-33.0	30.0	2.49e+02	1.55e+19	2.91e-08	1.45e+03
-33.0	35.0	1.89e+02	1.21e+19	1.88e-10	4.56e+02
-33.0	40.0	1.43e+02	9.33e+18	4.07e-12	4.58e+02
-33.0	45.0	1.07e+02	7.00e+18	5.62e-13	5.35e+02
-43.0	20.0	4.19e+02	2.37e+19	1.43e-06	2.57e+02
-43.0	25.0	3.25e+02	1.94e+19	2.68e-07	2.89e+02
-43.0	30.0	2.49e+02	1.55e+19	1.14e-08	3.31e+02
-43.0	35.0	1.89e+02	1.21e+19	4.38e-11	3.83e+02
-43.0	40.0	1.43e+02	9.33e+18	2.29e-12	4.49e+02
-43.0	45.0	1.07e+02	7.00e+18	3.27e-13	5.33e+02

aerosol loading is required to model the continuum at wavelengths longer than 220 nm. Assuming that the refractive index derived from this portion of the spectrum does not vary with wavelength, the optical depth of the aerosols at wavelengths shorter than 220 nm becomes negligible compared with that of NH_3 absorption (with the possible exception of the absorption cross section minima at ~210 and ~215 nm) and Rayleigh scattering. Thus, the NH_3 distribution derived by including this haze is identical to that derived assuming no aerosols. Although the existence of a distribution of aerosols with optical properties that would have a larger impact on the derived ammonia profiles while also mimicking the observed spectra has not been ruled out, we feel that assuming minimal aerosol influence to be reasonable given the lack of physical constraints on the aerosol properties. Work is currently in progress to determine the range of aerosol properties that can be tolerated by the FOS spectra.

Figures 6 and 7 show the eddy mixing profiles which are necessary, within the context of our one-dimensional photochemical model, to produce the required NH_3 distribution for each region. The strongest mixing is observed at the Equator and 6°S during Cycle 2, while the weakest is at 48°S during Cycle 2. Like NH_3, one can see a strong variation of the vertical mixing with latitude, where, for a given altitude, the values can vary by several orders of magnitude. For both vertical mixing and ammonia abundance, the variation with latitude is not monotonic, but depends on the latitude and feature observed; e.g., compare SEB and GRS. This suggests that regional convective activities may dominate the structure of the atmosphere near the tropopause rather than only solar-influenced variations, e.g., photolysis and UV/visible heating, which would tend to vary monotonically about the subsolar point.

These eddy profiles exhibit the properties of having a relatively large value of K (>1000 cm^2 s^{-1}) below the 500-mbar level, above which they drop to a minimum (<80 cm^2 s^{-1}), followed by an increase in value at still lower pressures until it merges with an eddy profile having a power-law density dependence which is extrapolated from Voyager results (Atreya *et al.*, 1981). One possible physical interpretation of this ledge-like structure is that it represents a transition from an unstable region to a stable region, much like that which occurs near the Earth's tropopause.

It is interesting to note that for 43°S, a mixing profile of this type was inadequate in generating an ammonia profile that fit the data. For this region, it was found that a profile that simply follows a power law, e.g., $n^{-0.6}$, gives a better fit of the FOS spectrum. With this profile, the mixing drops to low values (~100 cm^{-2} s^{-1}). Values such as this may be an indication that bulk motions may play a stronger role in determining the vertical motions as opposed to turbulent processes and that K may not be the most appropriate parameter to use in the modeling. Another possibility is that aerosols may play a stronger role at this latitude and tend to obscure some of the ammonia actually present in this region.

As mentioned above, several observations, e.g., GRS, 7°N, and 10°S, actually require the abundance of NH_3 to be lower than the nominal saturated profile for pressures greater than 250 mbar. For each region, the synthetic spectra generated by

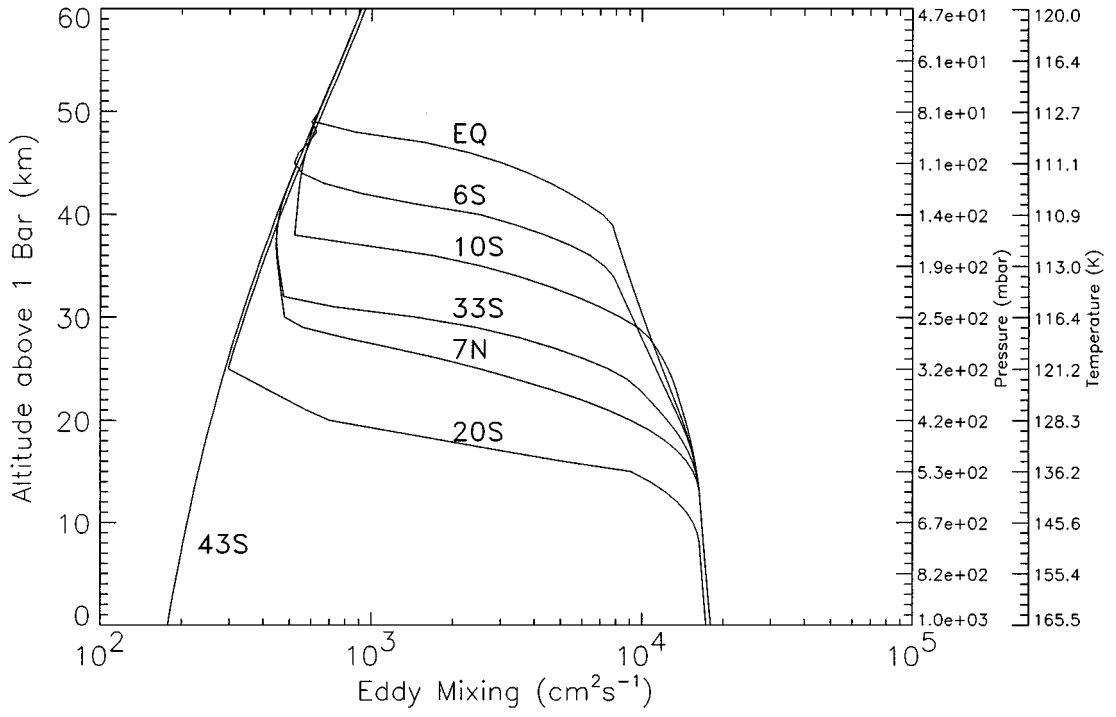

FIG. 6. Variation of the eddy mixing profiles with altitude for latitudes in the southern hemisphere of Jupiter.

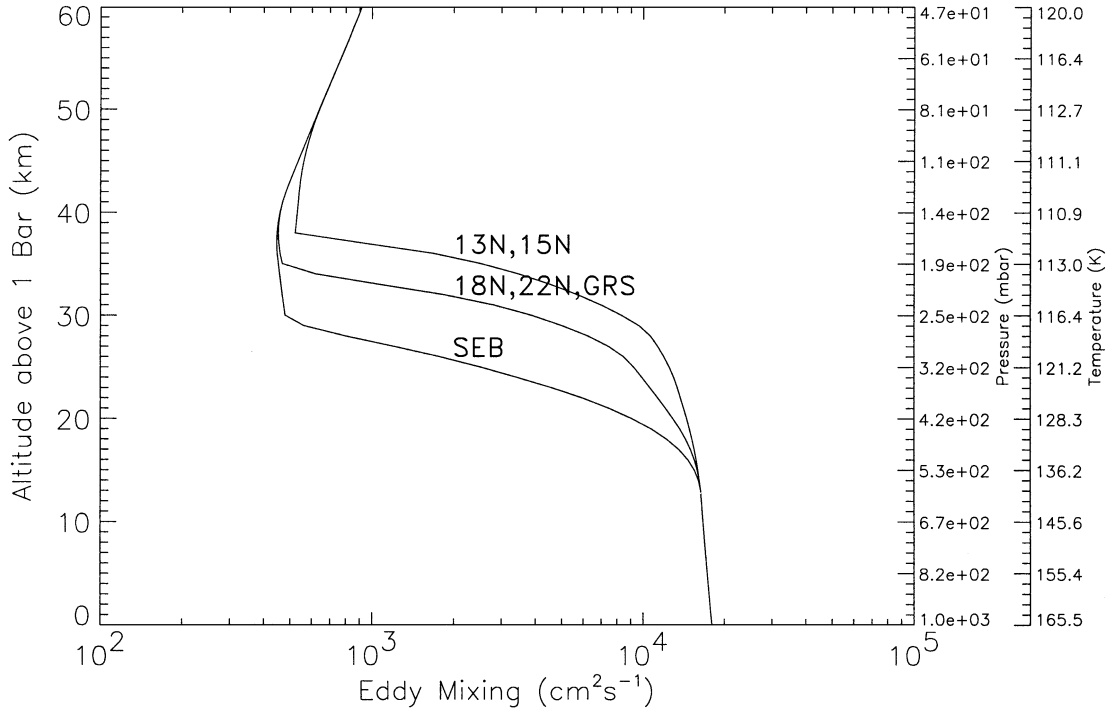

FIG. 7. Variation of the eddy mixing over the Great Red Spot and the South Equatorial Belt. Results derived from the Cycle 1 northern hemisphere data are also shown for comparison.

constraining ammonia to the nominal saturated profile all lack the contrast of the NH_3 bands seen in the FOS observations. However, reducing the NH_3 mixing ratio at pressures greater than 250 mbar will act to raise the continuum of the synthetic spectra. Adjusting the mixing ratio above this level will give the contrast of the ammonia spectral features. One possible way to accomplish this is to lower the temperature of the atmosphere, thus reducing the amount of available ammonia at this level. Since the final ammonia profile is a result of a balance between mixing, photolysis, and condensation, the eddy mixing can still be used to adjust the ammonia profile to give a fit of the FOS data. In this analysis, the reason for the decrease in NH_3 abundance has thus been interpreted as a local temperature decrease of roughly 2.5–7.5 K relative to the nominal model atmosphere, which is feasible based on Voyager observations (Gierasch *et al.* 1986). However, this does not rule out the presence of an unknown dynamical/chemical process, e.g., heterogeneous chemistry, which acts to subsaturate the NH_3 relative to the nominal profile. Either process could be true of the GRS region, which has been observed to be more dynamically active region with both colder temperatures and a larger abundance of aerosols than surrounding regions.

Also one should note that 7°N is depleted of ammonia. Again, this may correspond to the observed region having a colder temperature. However, since the latitude is the home of several "hot spots," the observation may actually correspond to one such region in which the ammonia is depleted by some dynamical mechanism not considered here. Furthermore, radio observations (dePater, 1986) indicate that ammonia is depleted near this latitude.

Spectra of 43°N, 61°N, and 66°N taken during Cycle 1 were shown in Paper I to be fairly flat over the entire wavelength range with little to no discernible spectral signature of NH_3. These spectral characteristics were best interpreted to be caused by hazes at altitude levels where they can obscure NH_3 that is present lower in the atmosphere. In the Cycle 2 observations presented here, we see that the 43°N spectrum has a much higher continuum (in fact larger than that near the equator) and contains much stronger NH_3 absorption features than its counterpart taken the previous year (Fig. 1). In fact, when compared with albedos along the central meridian obtained from HST Wide Field and Planetary Camera (WF/PC2) images (Fig. 8), the 43°N FOS spectrum is shown to be quite anomalous with an albedo of ∼0.4 at 230 nm, whereas the WF/PC2 images never exceed ∼0.25 due to hazes (Friedson *et al.* 1998).

Due to the combination of the single scattering albedo of a Rayleigh–Raman scattering [∼0.93 at 210 nm (Ford and Browne 1973)] atmosphere and the lower zenith angles of the incoming and outgoing radiation compared with those at lower latitudes, the continuum level of a pure Rayleigh–Raman scattering atmosphere (Fig. 9a) lies just above the observed spectrum, where it can be see that the albedo of the synthetic spectrum is roughly 0.45. This sets an upper limit for the radiation leaving the atmosphere. Adding NH_3 will lower the albedo even further (Figs. 9b, 9c). However, for all NH_3 profiles considered, no satisfactory fits to the data could be obtained as either the synthetic spectra had

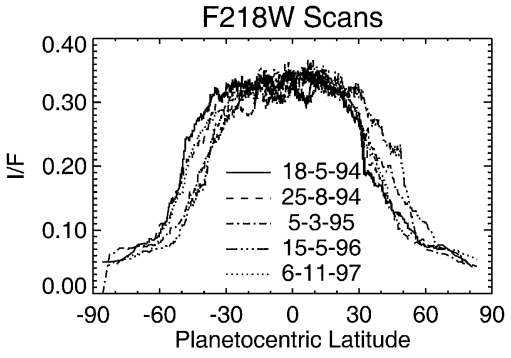

FIG. 8. Albedo along the central meridian at an effective wavelength of 230 nm. These scans were obtained from HST Wide Field and Planetary Camera 2 images in the F218 filter on several dates (Friedson *et al.*, 1998). One can see that for latitudes larger than 30°N, the albedo drops from typical midlatitude values of ~0.33.

only weak NH_3 signatures or the continuum level was lower than that of the observations. Thus, to obtain a signature of NH_3 required to match the FOS spectrum at 43°N, our single scattering albedo must be larger. One way to accomplish this may be to add aerosol particles that scatter brightly relative to the ambient atmosphere in the ultraviolet.

While our main goal in this paper is not to extract aerosol information to determine what kind of aerosol properties are required for 43°N, we have nevertheless attempted to fit the 43°N albedo with various combinations of the average particle size, altitude distributions, and refractive indices (1.4-*i*k, where *k* is the complex index of refraction) for the aerosols. It should be stressed that the inclusion of aerosols introduces many free parameters that are not well constrained by the data. Since the radiative properties of the aerosol particles affect the overall radiative balance of the atmosphere and seem to play a larger role at high latitudes, this non-uniqueness may have an impact on the derived ammonia distribution. Our simulations of the 43°N spectra indicate that small particles (<0.001 μm) must have very low absorption properties ($k < 10^{-7}$) in order to yield a single scattering albedo to make the synthetic albedo bright enough. Larger particles (~0.01 μm) allow for an imaginary index of refraction which varies linearly with wavelength from $k \sim 10^{-4}$ at 220 nm to $k \sim 10^{-5}$ at 190 nm. Larger particle sizes will in general allow for larger values of k. It should be noted that using the mean particle size, altitude distribution of aerosols, and imaginary index of refraction of 0.045 derived by Moreno and Sedano (1997) for 48°N, results in far too much absorption and consequently a very low albedo (<0.05 at 210 nm). Such values with some adjustment may be used in describing the Cycle 1 43°N spectra, but not the Cycle 2 43°N spectrum. The exact reason for the discrepancies of the 43°N spectra is unknown at this time and is being investigated further.

DISCUSSION

A number of other observational studies in the UV and IR exist with which our results may be compared. Direct comparison can be made with the results derived from UV spectra taken with the

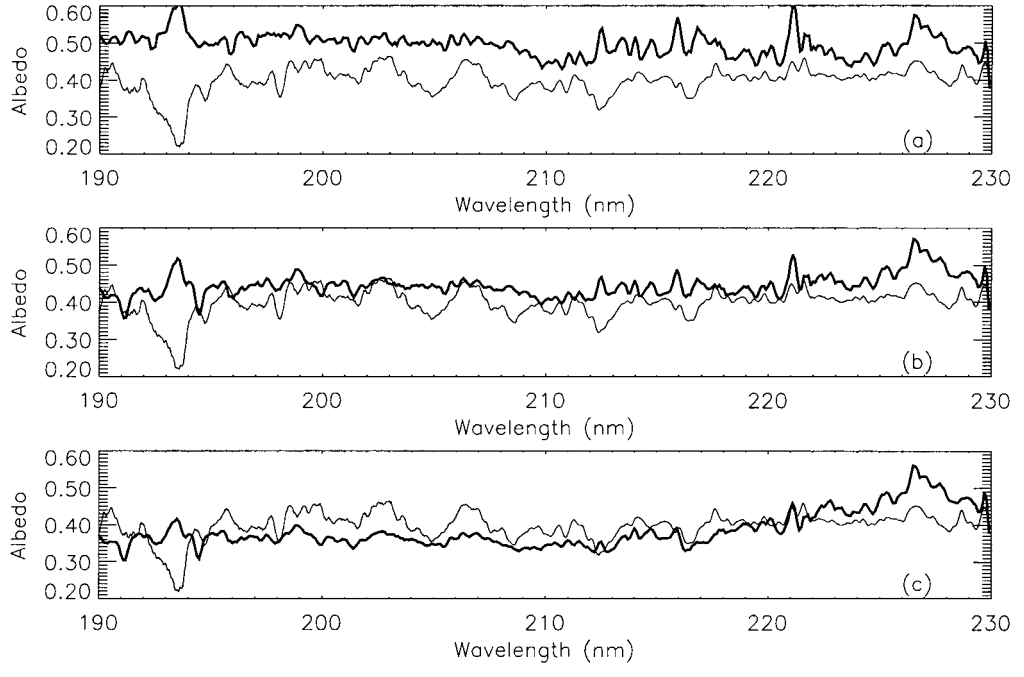

FIG. 9. Cycle 2 43°N reflectance. These panels illustrate the difficulty in fitting synthetic spectra to that of 43°N. (a) Synthetic spectrum (bold) for a clear Rayleigh–Raman scattering atmosphere with no absorbers. (b, c) Synthetic spectra (bold) resulting from two different profiles of ammonia. While the continuum level can be matched, no runs yielded an ammonia profile that can mimic individual ammonia lines.

International Ultraviolet Explorer (IUE) satellite (Combes *et al.* 1981, Wagener *et al.* 1985, 1986). These observations compare the GRS, the South Tropical Zone (STZ), and the center of the jovian disk (equator), albeit with poorer spatial (5–6 sec) and spectral (∼1 nm) resolution. Combes *et al.* (1981) attempted fitting several ammonia profiles, but uncertainties in the IUE data allowed for a large range of uncertainty in their results. Wagener *et al.* (1986) found that the NH_3 mixing ratio over the GRS is enhanced by a factor of 3–10 in the range 80–125 mbar compared with the STZ and the disk center (see Fig. 5 which reproduces their altitude profiles). In general, we obtain smaller mixing ratios than those derived from the IUE measurements at a given altitude level. These differences can be partially attributed to the use of different absolute calibration standards for the IUE and FOS spectra, since the brighter FOS albedos imply the ammonia should be confined deeper in the atmosphere. Using IUE-based calibrations provided by STScI, as done in Paper I, the FOS spectra do indeed give comparable results. However, we find that we need less NH_3 in the GRS region than the surrounding regions, as opposed to a larger abundance inferred from the IUE data. The source of the difference may lie in a temporal/spatial variation between their observations and ours. Furthermore, like Wagener *et al.* (1985), since the NH_3 (and PH_3) opacity decreases rapidly with increasing wavelengths, we find that an additional absorber, quite possibly an aerosol, is needed to account for the continuum at wavelengths longer than 220 nm.

Several infrared spectral lines of NH_3 were observed by Lara *et al.* (1998) with the Infrared Telescope Facility (IRTF) in January 1991 for the southern hemisphere of Jupiter from 10°S to 36°S at several lines of longitude. Their data suggest that a longitude dependence may exist in the mixing ratio (see their Fig. 7). Since our FOS measurements are along the CML at somewhat random longitudes, it is difficult to totally correlate our results with those of Lara *et al.* Nevertheless, several comparisons can be made. For the 240-mbar pressure level, at several longitudes Lara *et al.* determine that the NH_3 mixing ratio peaks at 15–18°S and decreases as one proceeds further south toward 30–35°S latitude where the NH_3 abundance is roughly 40 times lower. This is in agreement with the general trend of decreasing ammonia as we move from the equator toward the poles derived from the FOS data (compare EQ to 33°S in Fig. 4). The IRTF-derived profiles tend to yield lower NH_3 abundances than our results at pressure levels of 100–275 mbar where most of the UV photons originate (compare their 10°S, 287°W and 20°S, 287°W in Fig. 7 of Lara *et al.* to ours). This discrepancy may be due to their lower sensitivity to pressure levels less than 240 mbar (see Fig. 1 of Lara *et al.*) or our absolute calibrations.

Griffith *et al.* (1992) derived the NH_3 and PH_3 abundances over the GRS and the surrounding STZ from observations taken with the Voyager Infrared Imaging Spectrometer (IRIS). At 300 mbar, NH_3 was found to be depleted by 75% over the GRS compared with the STZ, for which they obtained a mixing ratio of 1.5×10^{-6}. Unfortunately, the UV observations do not probe as deep as these IR observations due to the physical limitations of Rayleigh–Raman scattering and the rapidly increasing ammonia opacity. However, above 300 mbar, we reach the same conclusion that the NH_3 mixing ratio over the GRS is depleted relative to most other regions including the SEB and 20°S regions.

The IRTF data of Lara *et al.* (1998) for the GRS imply that the NH_3 distribution at 380 mbar does not vary when compared with other longitudes along the GRS latitude (∼21°S), essentially in agreement with the findings of the Griffith *et al.* IRIS analysis. Lara *et al.* note that for the GRS, the ammonia mixing ratio at 380 mbar is 30% higher (only marginally greater than their uncertainties) compared with neighboring latitudes along the same longitude (∼27°W, System II). At this pressure level, their NH_3 mixing ratio peaks again near 13°S and 36°–39°S with abundances greater than at the GRS latitude. At longitude 110°, while the NH_3 abundance is not much more different than for the GRS latitude, the NH_3 abundance peaks between 27°S and 30°S with an abundance roughly twice greater than the GRS abundance. These results indicate that the GRS does not stand out as an exceptional region. Furthermore, comparison with the IRTF SEB results at the same pressure levels indicates that ammonia can exhibit local variations illustrating that caution should be used in making a general statement regarding the behavior of ammonia from our SEB and GRS results. Unfortunately, no IR observations of the 240-mbar pressure level for which a more direct comparison may be made in the photolysis region were taken along the GRS longitude. Observations of such kind would be highly desirable for comparison and for drawing a more complete picture of the behavior of ammonia over the GRS.

Both the Griffith *et al.* and Lara *et al.* results indicate that the NH_3 profile is subsaturated (15–100% humidity) at 380 mbar over most of the regions observed. Most of our model runs show NH_3 to be subsaturated just below the tropopause (located near 100 mbar), which we attribute to photolysis. We are not able to directly determine whether this is the case at the pressure levels observed at infrared wavelengths (>300 mbar) which lie below the levels observed with the FOS, since the NH_3 opacity rises rapidly with increasing pressure. However, the ammonia profiles at pressures where the FOS data originate are constrained (through our photochemical model) by the mixing ratio of ammonia deeper in the atmosphere, where it is limited by the NH_3 saturation vapor pressure. To test the sensitivity of our fits to the degree of ammonia saturation, cases for 50%, 100% (defined to be the saturation ammonia vapor pressure of the model atmosphere), and 150% saturation for the case of 13°N were run. For supersaturation, an unlikely possibility, the model allows too much ammonia to be present in the photolysis region since the saturation effect becomes less constraining. This increased ammonia gives a lower continuum albedo over the entire wavelength range making it impossible to fit the data. On the other hand, saturation of 50% leads to a minimal increase in the continuum beyond 220 nm and leaves wavelengths <220 nm unaffected. Thus, the dominant effect of the degree of saturation in the lower atmosphere is the adjustment of the UV continuum level which cannot be uniquely distinguished from the effect of

absorption by aerosols without further observational constraints. From these results, we can safely rule out supersaturation of ammonia, but the results are relatively insensitive to moderate subsaturation. Exceptions to these cases of moderate subsaturation are the instances where a larger depletion (due to lower temperatures) of NH_3 is required to satisfactorily reproduce the spectra (Figs. 4, 5).

CONCLUSIONS

The ultraviolet observations presented in this paper have been used to derive the altitude distribution of ammonia and the vertical mixing coefficient at several latitudes in the northern and southern hemispheres of Jupiter. A direct observation of the Great Red Spot and the nearby South Equatorial Belt, which forms its northern boundary, were also examined. The albedo variations of the FOS are due not only to the geometrical changes in the solar and Earth zenith angles, but also to real changes in the vertical distribution of NH_3 with latitude (Figs. 4, 5).

Within the context of a one-dimensional photochemical model, the strength of eddy mixing also needs to vary with latitude (Figs. 6, 7) to generate the vertical distributions of NH_3. It is obvious from these observations that the variations with latitude are not monotonic. Instead, there is a strong variability that is indicative of local changes in the strength of convective activity. How this might correlate with the belt-zone structure and local dynamics observed lower in the atmosphere, i.e., near the cloud tops, requires further observations with finer spatial resolution and latitude sampling, along with more realistic modeling of the dynamics and photochemistry of the lower stratosphere and upper troposphere of Jupiter.

Comparison with data taken in the infrared indicates several discrepancies which may be due to longitudinal and/or time variations or modeling of data. The most important difference is in the NH_3 mixing ratios obtained for the southern hemisphere which our data suggest are larger between roughly 150 and 300 mbar compared with those obtained from the IR measurements. Compared with other nearby regions, IR observations of the GRS tend to indicate either a slightly greater ammonia mixing ratios or even a depletion over the GRS. We are in agreement with the latter. This goes against physical intuition based on arguments of greater upwelling expected in the GRS region yielding a larger ammonia abundance. However, more efficient condensation processes in this region may be key to resolving this paradox. Combined analysis of simultaneous UV and IR observations of the same regions (latitude and longitude) measuring both ammonia and temperature may aid in resolving the differences between the UV and IR results and further explaining the physical phenomena governing this relatively unexplored region of the jovian atmosphere.

APPENDIX: RAMAN SCATTERING

Raman scattering occurs when a photon hits a molecule and causes the molecule to enter a different rotational and/or vibrational energy state without destruction of the photon (e.g., Cochran and Trafton 1978). This process either takes energy away from the photon or causes it to gain energy depending on the nature of the molecular transition. Thus the photon effectively shifts to a longer or shorter wavelength, respectively. The number of photons shifted depends on the cross section for each Raman transition compared with those monochromatically (Rayleigh) scattered or absorbed and the population of the initial energy states of the molecule. For Jupiter and Saturn, most of the molecular hydrogen in the troposphere resides in the $j = 0$ (*ortho*) and $j = 1$ (*para*) rotational states of the lowest vibrational energy state ($v = 0$) due to the low temperatures (<200 K) in the tropospheres of the Giant Planets. Thus, most often hydrogen molecules are excited to higher energy states and the photon is shifted to longer wavelengths. Comparatively, and fortunately for quick numerical calculations, very few transitions toward shorter wavelengths occur.

To treat Raman scattering, we must add a source term to the radiative transfer equation (RTE) to account for the appearance of scattered radiation into the wavelength interval of interest and a loss term for those photons scattered out of this wavelength bin. The radiative transfer equation then takes the form

$$\begin{aligned}
\mu \frac{dI_\lambda(z,\Omega)}{dz} d\lambda &= -\sum_i n_i \left(\sigma_{i\lambda}^{\text{abs}} + \sigma_{i\lambda}^{\text{scat}} + \sum_k \sigma_{ik\lambda}^{\text{Raman}}\right) I_\lambda(z,\Omega)\, d\lambda \\
&\quad + \frac{1}{4\pi} \sum_i n_i \sigma_{i\lambda}^{\text{scat}} \oint_{\Omega'} P_{i\lambda}(z,\Omega,\Omega') I_\lambda(z,\Omega')\, d\Omega' d\lambda \\
&\quad + \frac{1}{4\pi} \sum_i \sum_k n_i \sigma_{ik\lambda'}^{\text{Raman}} \delta\left(\frac{1}{\lambda} = \frac{1}{\lambda'} - \frac{\Delta\nu_k}{c}\right) \\
&\quad \times \oint_{\Omega'} P_{ik\lambda'}^{\text{Raman}}(z,\Omega,\Omega') I_{\lambda'}(z,\Omega')\, d\Omega' d\lambda', \qquad \text{(A1)}
\end{aligned}$$

where the i sums are over all gaseous and aerosol species (*ortho*- and *para*-hydrogen are treated as individual species here); the k sums are over all Raman transitions of the ith species; I_λ is the intensity; z is the altitude; μ is the angle with respect to the vertical; n_i is the number density; $\sigma_{i\lambda}^{\text{abs}}$ and $\sigma_{i\lambda}^{\text{scat}}$ are the cross sections for photoabsorption and scattering, respectively; $\sigma_{ik\lambda}^{\text{Raman}}$ is the Raman scattering cross section; $\Delta\nu_k$ is the frequency shift of the kth Raman transition; Ω is the directional (solid) angle; λ and λ' are the final and initial wavelengths, respectively; and the $P_{i\lambda}$ are phase functions. δ is the Dirac delta function.

To solve this equation, the last term on the right-hand side must be transformed from the wavelength interval $d\lambda'$ to the interval $d\lambda$. (Note that these intervals are infinitesimals. For discrete calculations, the intervals must be small enough such that the following arguments hold.) These intervals can be easily related, since barring any broadening mechanism the energy interval, dE, in which the photon resides, is constant during a Raman

shift. Equating the energy intervals around the original and shifted wavelengths, i.e., $dE = dE'$, we obtain the relationship

$$\frac{d\lambda}{\lambda^2} = \frac{d\lambda'}{(\lambda')^2}. \tag{A2}$$

The radiative transfer equation (A1) then becomes

$$\begin{aligned}\mu \frac{dI_\lambda(z,\Omega)}{dz}\, d\lambda &= -\sum_i n_i \left(\sigma_{i\lambda}^{\text{abs}} + \sigma_{i\lambda}^{\text{scat}} + \sum_k \sigma_{ik\lambda}^{\text{Raman}}\right) I_\lambda(z,\Omega)\, d\lambda \\ &+ \frac{1}{4\pi} \sum_i n_i \sigma_{i\lambda}^{\text{scat}} \oint_{\Omega'} P_{i\lambda}(z,\Omega,\Omega') I_\lambda(z,\Omega')\, d\Omega'\, d\lambda \\ &+ \frac{1}{4\pi} \sum_i \sum_k n_i \sigma_{ik\lambda'}^{\text{Raman}} \delta\left(\frac{1}{\lambda} = \frac{1}{\lambda'} - \frac{\Delta\nu_k}{c}\right) \\ &\times \oint_{\Omega'} P_{ik\lambda'}^{\text{Raman}}(z,\Omega,\Omega') I_{\lambda'}(z,\Omega')\, d\Omega' \left(\frac{\lambda'}{\lambda}\right)^2 d\lambda. \end{aligned} \tag{A3}$$

Dividing by $d\lambda$ will give us the usual form of the radiative transfer equation with an "absorption" term accounting for the loss of shifted photons and an "emission" term accounting for the Raman scattered light from other wavelengths. The "emission" term will make the absolute intensity, and hence albedo, dependent on the strength of the solar spectrum at shorter wavelengths, which effectively modifies the continuum and may produce "ghost" features of solar lines (Cochran and Trafton 1978).

Raman scattering cross sections have been obtained from Ford and Browne (1973) for a total of six transitions of H_2 corresponding to the two lowest rotational shifts in the ground vibrational state and four rovibrational transitions from the ground vibrational state to the first vibrational state, i.e., $S(0)$, $S(1)$, (1–0) $S(0)$, (1–0) $S(1)$, (1–0) $Q(0)$, and (1–0) $Q(1)$. It is important to note that, since the number of photons is conserved in a Raman transition, the intensity and Raman scattering cross sections must be in terms of photons transferred and not energy radiated (Wallace 1972), which is typically calculated in theoretical calculations (e.g., Ford and Browne 1972). Thus, these cross sections were then scaled by λ/λ' to convert to photons transferred (Harney *et al.* 1975). An *ortho* : *para* ratio of 3 : 1 has been chosen corresponding to a "normal" distribution of states. Although deviations have been observed in the jovian atmosphere (e.g., Conrath and Gierasch 1984), we do not expect our derived NH_3 profiles to be very sensitive to this due to several factors: the strength of NH_3 opacity over Raman scattering, the uncertainty in the fine structure of the solar spectrum at the time of the observations, the effective resolution of the FOS albedo (~0.34 nm), and the neglect of polarization in our radiative transfer calculations, which can amount to a 10% error.

ACKNOWLEDGMENTS

S.K.A. acknowledges support from Grant NAG5-4589 received from NASA's Planetary Atmospheres Program. The observations used in this paper was made possible by NASA through the Space Telescope Science Institute (Proposal ID 3887), which is operated by the Association of Universities for Research in Astronomy, Inc., under NASA Contract NAS5-26555.

REFERENCES

Atreya, S. K., T. M. Donahue, and M. C. Festou 1981. Jupiter: Structure and composition of the upper atmosphere. *Astrophys. J.* **247**, L43–L47.

Chen, F., D. L. Judge, C. Y. R. Wu, J. J. Caldwell, H. P. White, and R. Wagener 1991. High-resolution, low temperature photoabsorption cross sections of C_2H_2, PH_3, AsH_3, and GeH_4, with applications to Saturn's atmosphere. *J. Geophys. Res.* **96**, 17,519–17,527.

Chen, F. Z., D. L. Judge, C. Y. R. Wu, and J. Caldwell 1999. Low and room temperature photoabsorption cross section of NH_3 in the UV region. *Planet. Space Sci.* **47**, 261–266.

Cochran, W. D., and L. M. Trafton 1978. Raman scattering in the atmospheres of the major planets. *Astrophys. J.* **219**, 756–762.

Combes, M., R. Courtin, J. Caldwell, T. Encrenaz, K. H. Fricke, V. Moore, T. Owen, and P. S. Butterworth 1981. Vertical distribution of NH_3 in the upper jovian atmosphere from IUE observations. *Adv. Space Res.* **1**, 169–175.

Conrath, B. J., and P. J. Gierasch 1984. Global variation of the para hydrogen fraction in Jupiter's atmosphere and implications for dynamics on the outer planets. *Icarus* **57**, 184–204.

Cunningham, C. C., and J. J. Caldwell 1993. Grating scatter in the HST Faint Object Spectrograph. In *Calibrating the Hubble Space Telescope* (J. C. Blades and S. J. Osmer, Eds.), pp. 199–208. Space Telescope Science Institute, Baltimore.

Dashevsky, I., and J. J. Caldwell 1998. Atmospheric structure of Jupiter from HST UV center and limb observations. *Bull. Am. Astron. Soc.* **30**, 1067.

de Pater, I. 1986. Jupiter's zone-belt structure at radio wavelengths. II. Comparison of observations with model atmosphere calculations. *Icarus* **68**, 344–365.

Edgington, S. G., S. K. Atreya, L. M. Trafton, J. J. Caldwell, R. F. Beebe, A. A. Simon, R. A. West, and C. Barnet 1997. On the latitude variation of ammonia, acetylene, and phosphine altitude profiles on Jupiter from HST Faint Object Spectrograph observations. *Icarus* **133**, 192–209.

Ford, A. L., and J. C. Browne 1973. Rayleigh scattering cross sections for the hydrogen molecule. *At. Data* **5**, 305–313.

Ford, H. C. 1985. *Faint Object Spectrograph Instrument Handbook*. Space Telescope Science Institute, Baltimore.

Friedson, A. J., R. A. West, A. K. Hronek, N. A. Larsen, and N. Dalal 1998. Transport and mixing in Jupiter's stratosphere inferred from Comet S-L9 dust migration. *Icarus* **138**, 141–156.

Gierasch, P. J., B. J. Conrath, and J. A. Magalhães 1986. Zonal mean properties of Jupiter's upper troposphere from Voyager infrared observations. *Icarus* **67**, 456–483.

Griffith, C. A., B. Bézard, T. Owen, and D. Gautier 1992. The tropospheric abundances of NH_3 and PH_3 in Jupiter's Great Red Spot from Voyager IRIS observations. *Icarus* **98**, 82–93.

Harney, R. C., J. E. Randolf, and F. P. Milanovich 1975. Relative Raman cross sections for the S(0) through S(4) rotational transitions in hydrogen. *Astrophys. J.* **200**, L179–L181.

Lara, L.-M., B. Bézard, C. A. Griffith, J. H. Lacy, and T. Owen 1998. High resolution 10-micron spectroscopy of ammonia and phosphine lines on Jupiter. *Icarus* **131**, 317–333.

Moreno, F., and J. Sedano 1997. Radiative balance and dynamics in the stratosphere of Jupiter: Results from a latitude-dependent aerosol heating model. *Icarus* **130**, 36–48.

Seiff, A., D. B. Kirk, T. C. D. Knight, L. A. Young, F. S. Milos, E. Venkatapathy, J. D. Mihalov, R. C. Blanchard, R. E. Young, and G. Schubert 1997. Thermal structure of Jupiter's upper atmosphere derived from the Galileo Probe. *Science* **276**, 102–104.

Van Hoosier, M. E., J.-D. F. Bartoe, G. E. Brueckner, and D. K. Prinz 1988. Absolute solar spectral irradiance 120 nm–400 nm (Results from the Solar Ultraviolet Spectral Irradiance Monitor—SUSIM—Experiment on board Spacelab 2). *Astro. Lett. Com.* **27**, 163–168.

Wagener, R., J. Caldwell, T. Owen, S.-J. Kim, T. Encrenaz, and M. Combes 1985. The jovian stratosphere in the ultraviolet. *Icarus* **63**, 222–236.

Wagener, R., J. Caldwell, and T. Owen 1986. Constraints on the NH_3 and PH_3 distributions in the Great Red Spot. *Icarus* **66**, 188–191.

Wallace, L. 1972. Rayleigh and Raman scattering by H_2 in a planetary atmosphere. *Astrophys. J.* **176**, 249–257.